Auxiliary materials for “Porous fluid flow enables oceanic subduction initiation on Earth”

Diana Dymkova, Taras Gerya

October 22, 2013

Model design

Tectonic setup of two oceanic plates of contrasting ages juxtaposed through the transform fault [*Hall et al.*, 2003; *Gurnis et al.*, 2004] is shown on the Fig. 1a. Older plate (on the left) and younger plate (on the right) are separated by a wet transform zone denoted by a yellow color. All shades of blue indicate lithospheric plates and asthenospheric mantle (Table S2). Both plates are covered with 2 km of upper basaltic and 5 km of lower gabbroic crust. Wet transform is covered with 7 km of basalts. On the op, the whole system is covered with a 20 km low density and viscosity sea water layer (Table S2) to simulate the free surface *Schmeling et al.* [2008]; *Crameri et al.* [2012]. All the boundaries are free slip except the lower one which is permeable in the vertical direction.

The initial thermal structure is calculated according to the cooling ages of the plates using half-space model [*Turcotte and Schubert*, 2002]:

$$T = T_1 + (T_0 - T_1) \cdot \left(1 - erf\left(\frac{d}{2\sqrt{\kappa\tau}}\right)\right),$$

where T_0 = 273 K and T_1 = 1600 K is the surface and astenospheric mantle temperature, d is the depth, τ is the plate age and $\kappa = 10^{-6} m^2\ s^{-1}$ is thermal diffusivity. In order to provide the sufficient heat transfer from the plates' surface, sea water is prescribed with the thermal conductivity of two orders of magnitude higher then the one of the plates (Table S2).

Governing equations

The system of equations for fluid-filled matrix viscous flow is similar to existing approaches [*Stevenson and Scott*, 1991; *Connolly and Podladchikov*, 2000; *McKenzie*, 1984; *Morency et al.*, 2007] and reformulated for convenient implementation with our numerical technique. As a staring point of our model, we have taken the equation system of *Stevenson and Scott* [1991] with two-pressures approach (Eq. S1): one variable indicates the pressure in the solid phase and another for the fluid. The modification we have introduced is the use of total pressure (p_t) rather than fluid pressure (p_f) in the total momentum conservation equation written for the "bulk" material, i.e., porous solid matrix filled with the fluid [*Stevenson and Scott*, 1991; *Morency et al.*, 2007]. That means that in our hydro-thermo-mnechanical (HTM) approach we combine two parallel processes: visco-plastic flow of the "bulk" porous material and the corresponding fluid filtration.

Viscous compaction is represented by the porosity equation [e.g. *Connolly and Podladchikov*, 2000, 1998]:

$$\frac{D\ln(1-\varphi)}{Dt} = \frac{p_t - p_f}{\eta_{bulk}}, \tag{S1}$$

where φ is porosity, $p_{t,f}$ is total and fluid pressure, respectively, η_{bulk} is effective bulk viscosity of a porous fluid-filled matrix. This equation is solved separately from the coupled system of the complex fluid-solid flow.

In accordance with previously derived systems [*Morency et al.*, 2007], for the mass conservation expression we assume individual media incompressibility (though the bulk material, porous fluid-filled matrix, might be not conserved due to pore opening/closure). For our model we use Boussinesq approximation which is taken into account in many existing mantle convection models [*Moresi and Solomatov*, 1995; *Gerya and Yuen*, 2003; *Albers*, 2000; *Crameri et al.*, 2012] and where density is assumed to be constant in all terms except for buoyancy force. Thus, for both solid and fluid phase we have:

$$div(v^S) = -\frac{D(ln(1-\varphi))}{Dt},$$
$$div(v^D) = \frac{D(ln(1-\varphi))}{Dt},$$

where $v^{S,f}$ is solid and fluid velocities respectively, Darcy velocity $v^D = \varphi(v^f - v^S)$. Using the porosity evolution law (Eq. S1), mass conservation equations take the form:

$$div(v^S) = -\frac{p_t - p_f}{\eta_{bulk}}, \tag{S2}$$

$$div(v^D) = \frac{p_t - p_f}{\eta_{bulk}}. \tag{S3}$$

Darcy law describes the flow of the fluid through the porous medium:

$$v_x^D = -\frac{K}{\eta_f} \cdot \frac{\partial p_f}{\partial x}, \tag{S4}$$

$$v_y^D = \frac{K}{\eta_f} \cdot \left(\rho_f g_y - \frac{\partial p_f}{\partial y} \right), \tag{S5}$$

where K is matrix permeability, ρ_f and η_f is fluid density and viscosity respectively. Gravitational acceleration $\vec{g}$ is directed downward along the vertical y-axis, while x-axis in the model is horizontal, thus $g_y = 9.81\ m/s^2$.

After *Stevenson and Scott* [1991], momentum conservation equation for bulk material is written in the form of Stokes equation of viscous fluid flow in the gravity field, inertia terms are neglected (so-called "slow flow" approximation):

$$\frac{\partial \sigma'_{ij}}{\partial x_j} - \frac{\partial p^f}{\partial x_i} = -g_i \rho_t,$$

where σ'_{ij} is bulk deviatoric stress, and $\rho_t = \rho_s(1-\varphi) + \rho_f \varphi$ is bulk material density. Similarly to the previous work [*Stevenson and Scott*, 1991], deviatoric stress of the bulk material (porous fluid-filled matrix) is written in terms of strain rate components of the solid matrix:

$$\sigma'_{ij} = 2\eta \dot{\varepsilon}'^s_{ij} + \eta_{bulk} \dot{\varepsilon}^s_{kk} \delta_{ij},$$

where the first compound is a shear stress component and the second is volumetric stress component, η is effective shear viscosity of the porous fluid-filled matrix. Deviatoric strain rate components are calculated in terms of solid matrix velocities [e.g. *Gerya and Yuen*, 2003, 2007] as:

$$\dot{\varepsilon}'^s_{xx} = \frac{1}{2} \left(\frac{\partial v_x^S}{\partial x} - \frac{\partial v_y^S}{\partial y} \right),$$

$$\dot{\varepsilon}'^s_{yy} = \frac{1}{2} \left(\frac{\partial v_y^S}{\partial y} - \frac{\partial v_x^S}{\partial x} \right),$$

$$\dot{\varepsilon}'^s_{xy} = \frac{1}{2} \left(\frac{\partial v_x^S}{\partial y} + \frac{\partial v_y^S}{\partial x} \right).$$

Thus, using the equation of solid mass conservation Eq. S2 and expressions above for

$\dot{\varepsilon}'^{S}_{ii}$, we have:

$$\sigma'_{ij} = 2\eta\dot{\varepsilon}'^{S}_{ij} + \eta_{bulk} \cdot div(v^S)\delta_{ij} = 2\eta\dot{\varepsilon}'^{S}_{ij} + (p_f - p_t)\delta_{ij}, \tag{S6}$$

and distinct stress components can be rewritten as following:

$$\sigma'_{xx} = \eta \left(\frac{\partial v^S_x}{\partial x} - \frac{\partial v^S_y}{\partial y} \right) + p_f - p_t,$$

$$\sigma'_{yy} = \eta \left(\frac{\partial v^S_y}{\partial y} - \frac{\partial v^S_x}{\partial x} \right) + p_f - p_t,$$

$$\sigma'_{xy} = \eta \left(\frac{\partial v^S_x}{\partial y} + \frac{\partial v^S_y}{\partial x} \right).$$

After substituting these expressions, x- and y-Stokes equations take the form:

$$\frac{\partial}{\partial x}\left(\eta\left(\frac{\partial v^S_x}{\partial x} - \frac{\partial v^S_y}{\partial y}\right)\right) + \frac{\partial}{\partial y}\left(\eta\left(\frac{\partial v^S_x}{\partial y} + \frac{\partial v^S_y}{\partial x}\right)\right) - \frac{\partial p_t}{\partial x} = 0, \tag{S7}$$

$$\frac{\partial}{\partial y}\left(\eta\left(\frac{\partial v^S_y}{\partial y} - \frac{\partial v^S_x}{\partial x}\right)\right) + \frac{\partial}{\partial x}\left(\eta\left(\frac{\partial v^S_x}{\partial y} + \frac{\partial v^S_y}{\partial x}\right)\right) - \frac{\partial p_t}{\partial y} = -\rho_t g_y. \tag{S8}$$

The temperature equation in our model is implemented in Langrangian frame of reference [*Gerya and Yuen*, 2003] for the fluid-filled matrix in terms of temperature T and thermal conductivity k (internal heating terms are neglected):

$$\rho_t C_p \frac{DT}{Dt} = \frac{\partial}{\partial x}\left(k\frac{\partial T}{\partial x}\right) + \frac{\partial}{\partial y}\left(k\frac{\partial T}{\partial y}\right). \tag{S9}$$

Rheological model

The rheological model employed is non-Newtonian visco-plastic. Therefore, the deviatoric strain rate is composed of two terms:

$$\dot{\varepsilon}'_{ij} = \dot{\varepsilon}'_{ij(viscous)} + \dot{\varepsilon}'_{ij(plastic)},$$

where

$$\dot{\varepsilon}'_{ij(viscous)} = \frac{1}{2\eta}\sigma'_{ij},$$

$$\dot{\varepsilon}'_{ij(plastic)} = 0 \;\; for \;\; \sigma_{II} < \sigma_{yield},$$

$$\dot{\varepsilon}'_{ij(plastic)} = \chi \frac{\partial G}{\partial \sigma'_{ij}} = \chi \frac{\sigma'_{ij}}{2\sigma_{II}} \;\; for \;\; \sigma_{II} = \sigma_{yield},$$

$$G = \sigma_{II},$$

$$\sigma_{II} = \sqrt{\frac{1}{2}\sigma'_{ij}\sigma'_{ij}},$$

where σ'_{ij} is deviatoric stress component, σ_{yield} is brittle/plastic strength of bulk material (see below), σ_{II} is a second deviatoric stress invariant, G is plastic potential of yielding material [*Vermeer*, 1990], χ is plastic multiplier that at every time step satisfies the plastic yielding condition:

$$\sigma_{II} = \sigma_{yield}.$$

Brittle/plastic strength for interconnected fluid-filled matrix ($\varphi > 10^{-4}$) is calculated with fluid pressure weakening taken into account [*Ranalli*, 1995; *Rozhko et al.*, 2007]:

$$\sigma_{yield} = C + \gamma(p_t - p_f),$$

where C is residual rock strength at zero pressure. At low porosities ($\varphi < 10^{-4}$), pores are considered to be isolated and fluid pressure weakening is not applied.

The effective shear viscosity of the rocks depends on the stress, pressure and temperature. It is calculated from the rheological law [*Ranalli*, 1995; *Gerya*, 2010] defined through the experimentally determined flow law parameters:

$$\eta = (\sigma_{II})^{(1-n)} \frac{1}{2A_D} \cdot \exp\left(\frac{E_a + p_t V_a}{RT}\right)$$

where A_D is pre-exponential factor, E_a and V_a are activation energy and volume, n is the stress exponent, R is the gas constant.

Numerical solution

The original Matlab-code used for the experiments is based on conservative finite differences approach and is applied on a fully-staggered grid in combination with markers-in-cell technique [*Gerya and Yuen*, 2003, 2007]. Computational domain of 600 km x 250 km size has a uniform grid resolution of 1 km x 1 km and contains about 3.8 millions of randomly distributed Lagrangian particles (markers) to provide the transport of material properties, such as viscosity, density, porosity, permeability and rheological law parameters. By means of solid particles motion, the non-diffusive markers method advects the temperature field [*Gerya and Yuen*, 2003, 2007] where heat advection with fluid is neglected.

Our coupled HTM system of equations consists of solid and fluid mass conservation equations Eq. S2 and Eq. S3, bulk material momentum conservation equations Eq. S7 - S8 and Darcy fluid filtration equations Eq. S4 - S5. The amount of equations and variables in the coupled system can be decreased by combining the fluid conservation equation Eq. S3 and Darcy equations Eq. S4 - S5. If we differentiate the x-Darcy equation with respect to x, y-equation with respect to y and sum them together, we are left with:

$$\left(\frac{\partial v_x^D}{\partial x}+\frac{\partial v_y^D}{\partial y}\right)+\frac{\partial}{\partial x}\left(\frac{K}{\eta_f}\frac{\partial p_f}{\partial x}\right)+\frac{\partial}{\partial y}\left(\frac{K}{\eta_f}\frac{\partial p_f}{\partial y}\right)=\frac{\partial}{\partial y}\left(\frac{K}{\eta_f}\rho_f g_y\right),$$

from where, using the Eq. S3 and assumption of constant fluid density and viscosity, we get:

$$(p_t-p_f)\cdot\frac{\eta_f}{\eta_{bulk}}+\frac{\partial}{\partial x}\left(K\frac{\partial p_f}{\partial x}\right)+\frac{\partial}{\partial y}\left(K\frac{\partial p_f}{\partial y}\right)=\frac{\partial K}{\partial y}\rho_f g_y. \tag{S10}$$

Finally, system is composed of equation of the solid mass conservation Eq. S2, Stokes viscous flow of bulk material Eq. S7 - S8 and combined fluid continuity and fluid filtration equation Eq. S10. After obtaining a solution of this system in terms of variables p_t, p_f, $v^S_{x,y}$, we solve Eq. S1, S9 and S4, S5, the porosity evolution, temperature and Darcy equations, respectively.

Permeability of rocks

In our experiments, permeability of crustal and mantle rocks varies in the range between 10^{-16} and 10^{-21} m^2. Values of chosen interval are rather on the lower bound of what is typically measured in the laboratory experiments [e.g. *Brace*, 1984; *Fisher*, 1998; *Faul*, 1997] (e.g. $10^{-13}-10^{-18}$ m^2 for crustal basalts) or normally used for numerical models [e.g. *Faccenda et al.*, 2009; *Connolly et al.*, 2009; *Richard et al.*, 2006]. The relevance of low permeability for maintenance of elevated pore fluid pressure during geologically significant periods of time was emphasized in both experimental measurement studies [*Brace*, 1984; *Trimmer et al.*, 1980; *Brace*, 1980] and theoretical studies of abnormal fluid pressure in sedimentary, metamorphic and tectonic settings [*Neuzil*, 1995; *Walder and Nur*, 1984; *Bredehoeft and Hanshaw*, 1968; *Hanshaw and Bredehoeft*, 1968; *Wong et al.*, 1997]. Walder and Nur [*Walder and Nur*, 1984], in their studies of pore pressure development in the crust, derived that permeability required for retention of high porous pressure should be as low as $5\cdot10^{-20}-10^{-21}$ m^2. Bredehoeft and Hansaw [*Bredehoeft and Hanshaw*, 1968; *Hanshaw and Bredehoeft*, 1968] concluded that under conditions of absence or bareness of low permeable layers (e.g. clays) it is doubtful that anomalous pore pressures can be maintained for longer than a geologic instant. In similar extended studies of dehydration systems [*Wong et al.*, 1997], authors calculated the critical values of confining layer permeabilities required for maintenance of nearly lithostatic pore pressure for typical dehydration reactions. The values fall within the interval of $10^{-17} - 10^{-21}$ m^2 which is characteristic for argillaceous rocks [*Hanshaw and Bredehoeft*, 1968] and unfractured low-porosity crystalline rocks [*Walder and Nur*, 1984; *Brace*, 1980]. Even lower values (between 10^{-20} and 10^{-24} m^2) were reported for intact gneissic granite and intact and fractured gabbro [*Trimmer et al.*, 1980].

Considering that resolution of our model does not allow us to resolve complex layered structures on the crustal level, we assume reference permeability to be equally low for the large volumes of various lithologies. Although it is quite a rough approximation and does not allow for tracing certain complexities of geological environment, it is of crucial importance for building up the nearly lithostatic pore pressures and investigating the fluid weakening influence on the rocks in geological systems, allowing in present case, for subduction initiation and further lubrication driven by the pore pressure excess. It should also be mentioned that the permeability limits estimated for the spontaneous subduction initiation can notably widen in the case of induced subduction initiation [e.g. *Hall et al.*, 2003; *Gurnis et al.*, 2004] due to the porous fluid pressure increase caused by the initial compression of the plate boundary.

Another important feature is that spatial [*Rice*, 1992] and temporal [*Walder and Nur*, 1984] variation of permeability plays important role in the development of excess pore pressure. Thus, among two similar studies [*Hanshaw and Bredehoeft*, 1968; *Wong et al.*, 1997] of anomalous pore pressure in dehydrating systems, the one with variable porosity-dependent permeability [*Wong et al.*, 1997] shows $\sim 20\%$ less of pore pressure excess than the one with fixed permeability values. Therefore porosity-dependent permeability (Eq. 4) [e.g. *Wong et al.*, 1997; *Morency et al.*, 2007; *Connolly and Podladchikov*, 2000] recalculated at each time step is of particular importance for model development and evolvement of local fluid flow focussing phenomena such as shear bands hydration (Fig. S2 - S3).

References

Albers, M. (2000), A local mesh refinement multigrid method for 3d convection problems with strongly variable viscosity., *J. Comput. Phys.*, *160*, 126–150.

Brace, W. (1980), Permeability of crystalline and argillaceous rocks, *Int. J. Rock Mech. Min. Sci.*, *17*, 241–251.

Brace, W. (1984), Permeability of crystalline rocks - new insitu measurements, *J. Geophys. Res.*, *89*, 4327–4330.

Bredehoeft, J., and B. Hanshaw (1968), On the maintenance of anomalous fluid pressures: I thick sedimentary sequences, *Geol. Soc. Am. Bull.*, *79*, 1097–1106.

Connolly, J., and Y. Y. Podladchikov (1998), Compaction-driven fluid flow in viscoelastic rock, *Geodinamica Acta*, *11*(2-3), 55–84.

Connolly, J., and Y. Y. Podladchikov (2000), Temperature-dependent viscoelastic compaction and compartmentalization in sedimentary basins, *Tectonophysics*, *324*, 137–168.

Connolly, J., M. Schmidt, G. Solferino, and N. Bagdassarov (2009), Permeability of asthenospheric mantle and melt extraction rates at mid-ocean ridges, *Nature*, *462*, 209–U83.

Crameri, F., P. Tackley, I. Meilick, T. Gerya, and B. Kaus (2012), A free plate surface and weak oceanic crust produce single-sided subduction on earth, *Geophys. Res. Lett.*, *39*(L03306).

Faccenda, M., T. Gerya, and L. Burlini (2009), Deep slab hydration induced by bending related variations in tectonic pressure, *Nature Geoscience*, *2*(790-793).

Faul, U. (1997), Permeability of partially molten upper mantle rocks from experiments and percolation theory., *J. Geophys. Res.*, *102*, 10,299–10,311.

Fisher, A. (1998), Permeability within basaltic oceanic crust, *Rev. Geophys.*, *36*, 143–182.

Gerya, T. (2010), *Numerical Geodynamic Modelling*, 1 ed., Cambridge University Press.

Gerya, T., and D. Yuen (2003), Rayleigh-taylor instabilities from hydration and melting propel cold plumes at subduction zones, *Earth and Planetary Science Letters*, *212*, 47–62.

Gerya, T., and D. Yuen (2007), Robust characteristics method for modelling multiphase visco-elasto-plastic thermo-mechanical problems, *Phys. Earth Planet. Int.*, *163*, 83–105.

Gurnis, M., C. Hall, and L. Lavier (2004), Evolving force balance during incipient subduction, *Geochem. Geophys. Geosyst.*, *5*(Q07001).

Hall, C., M. Gurnis, M. Sdrolias, L. Lavier, and R. Mueller (2003), Catastrophic initiation of subduction following forced convergence across fracture zones, *Earth Planet. Sci. Lett.*, *212*, 15–30.

Hanshaw, B., and J. Bredehoeft (1968), On the maintenance of anomalous fluid pressures: II source layer at depth., *Geol. Soc. Am. Bull.*, *79*, 1107–1122.

McKenzie, D. (1984), The generation and compaction of partially molten rock, *J. Petrol.*, *25*, 713–765.

Morency, C., R. Huismans, C. Beaumont, and P. Fullsack (2007), A numerical model for coupled fluid flow and matrix deformation with applications to disequilibtium compaction and delta stability, *Jour. Geophys. Res.*, *112*(B10404).

Moresi, L., and V. Solomatov (1995), Numerical investigation of 2d convection with extremely large viscosity variations., *Phys. Fluids*, *7*, 2154–2162.

Neuzil, C. (1995), Abnormal pressures as hydrodynamic phenomena, *American Journal of Science*, *295*, 742–786.

Ranalli, G. (1995), *Rheology of the Earth*, Chapman and Hall, London.

Rice, J. (1992), *Fault mechanics and transport properties of rocks*, chap. Fault stress states, pore pressure distributions, and the weakness of the San Andreas fault, pp. 475–504, Academic, San Diego, Calif.

Richard, G., D. Bercovici, and S.-I. Karato (2006), Slab dehydration in the earth mantle transition zone, *Earth Planet. Sci. Lett.*, *251*, 156–167.

Rozhko, A., Y. Y. Podladchikov, and F. Renard (2007), Failure patterns caused by localized rise in pore-fluid overpressure and effective strength of rocks, *Geophys. Res. Lett.*, *34*(L22304).

Schmeling, H., A. Babeyko, A. Enns, C. Faccenna, F. Funiciello, T. Gerya, G. Golabek, S. Grigull, B. Kaus, G. Morra, S. Schmalholz, and J. van Hunen (2008), A benchmark comparison of spontaneous subduction models - Towards a free surface, *Phys. Earth Planet. Int.*, *171*, 198–223.

Stevenson, D., and D. Scott (1991), Mechanics of fluid-rock systems, *Annu. Rev. Fluid Mech.*, *23*, 305–39.

Trimmer, D., B. Bonner, H. Heard, and A. Duba (1980), Effect of pressure and stress on water transport in intact and fractured gabbro and granite., *Jour. Geophys. Res.*, *85*, 7059–7071.

Turcotte, D., and G. Schubert (2002), *Geodynamics*, 2nd ed., Cambridge University Press, Cambridge.

Vermeer, P. (1990), The orientation of the shear bands in biaxial tests., *Geotechnique*, *40*, 223–236.

Walder, J., and A. Nur (1984), Porosity reduction and crustul pore pressure development, *J. Geophys. Res.*, *89*, 11,539–11,548.

Wong, T.-F., S.-C. Ko, and D. Olgaard (1997), Generation and maintenance of pore pressure excess in a dehydrating system. 2 theoretical analysis., *J. Geophys. Res.*, *102*, 841–852.

Table S1: Legend of variables.

A_D	material constant $[MPa^{-n}s^{-1}]$
b	bulk exponent
C	residual rock strength at zero pressure $[Pa]$
C_p	isobaric heat capacity $[J\ kg^{-1}K^{-1}]$
E_a	activation energy $[kJ\ mol^{-1}]$
G	plastic potential $[Pa]$
g_y	gravitational acceleration $[m\ s^{-2}]$
K	permeability $[m^2]$
k	thermal conductivity $[W\ m^{-1}K^{-1}]$
n	stress exponent
p_f	fluid pressure $[Pa]$
p_s	solid pressure $[Pa]$
$p_t = (1-\varphi)p_s + \varphi p_f$	total pressure $[Pa]$
R	gas constant $[J\ mol^{-1}K^{-1}]$
T	temperature $[K]$
t	time $[s]$
V_a	activation volume $[J\ MPa^{-1}\ mol^{-1}]$
$v^D = \varphi\left(v^f - v^S\right)$	Darcy velocity $[m\ s^{-1}]$
v^f	fluid velocity $[m\ s^{-1}]$
v^S	solid velocity $[m\ s^{-1}]$
q_i	heat flux $[Wm^{-2}]$
γ	internal friction coefficient
$\dot{\varepsilon}'_{ij}$	deviatoric strain rate tensor component $[s^{-1}]$
φ	porosity
$\rho_f = 1000\ kg\ m^{-3}$	fluid density $[kg\ m^{-3}]$
ρ_s	solid density $[kg\ m^{-3}]$
$\rho_t = (1-\varphi)\rho_s + \varphi\rho_f$	total density $[kg\ m^{-3}]$
$\eta_{bulk} = \eta/\varphi^b$	effective bulk viscosity of fluid-filled matrix $[Pa\ s]$
$\eta_f = 10^{-3}\ Pa\ s$	fluid viscosity $[Pa\ s]$
η	effective shear viscosity of fluid-filled matrix $[Pa\ s]$
σ_{II}	second deviatoric stress tensor invariant $[Pa]$
σ'_{ij}	deviatoric stress tensor component $[Pa]$
σ_{yield}	plastic yield strength $[Pa]$

Table S2: Physical properties of the lithologies used in the experiments; other parameters for all the lithologies are: thermal expansion $\alpha = 3 \cdot 10^{-5}\ K^{-1}$, isobaric heat capacity $C_p = 1000\ J\ kg^{-1}\ K^{-1}$.

Rock type	Density *Turcotte and Schubert* [2002] kg/m^3	Porosity %	γ	C MPa	Thermal conductivity $W\ m^{-1}\ K^{-1}$	Flow law *Ranalli* [1995]
Upper basaltic crust	3100	0.5 - 3.0	0.2 - 0.6	1	1.18	Plagioclase An_{75}
Lower gabbroic crust	3150	0.5 - 1.0	0.6	1	1.18	Plagioclase An_{75}
Wet transform	3250	0.5 - 3.0	0.2 - 0.6	1	0.73	Wet olivine
Lithospheric mantle	3300	~ 0	0.6	1	0.73	Dry olivine
Astenospheric mantle	3300	~ 0	0.6	1	0.73	Dry olivine
Sticky water	1000	10.0	0.0	10^4	300	Newtonian, $10^{-18} Pa \cdot s$

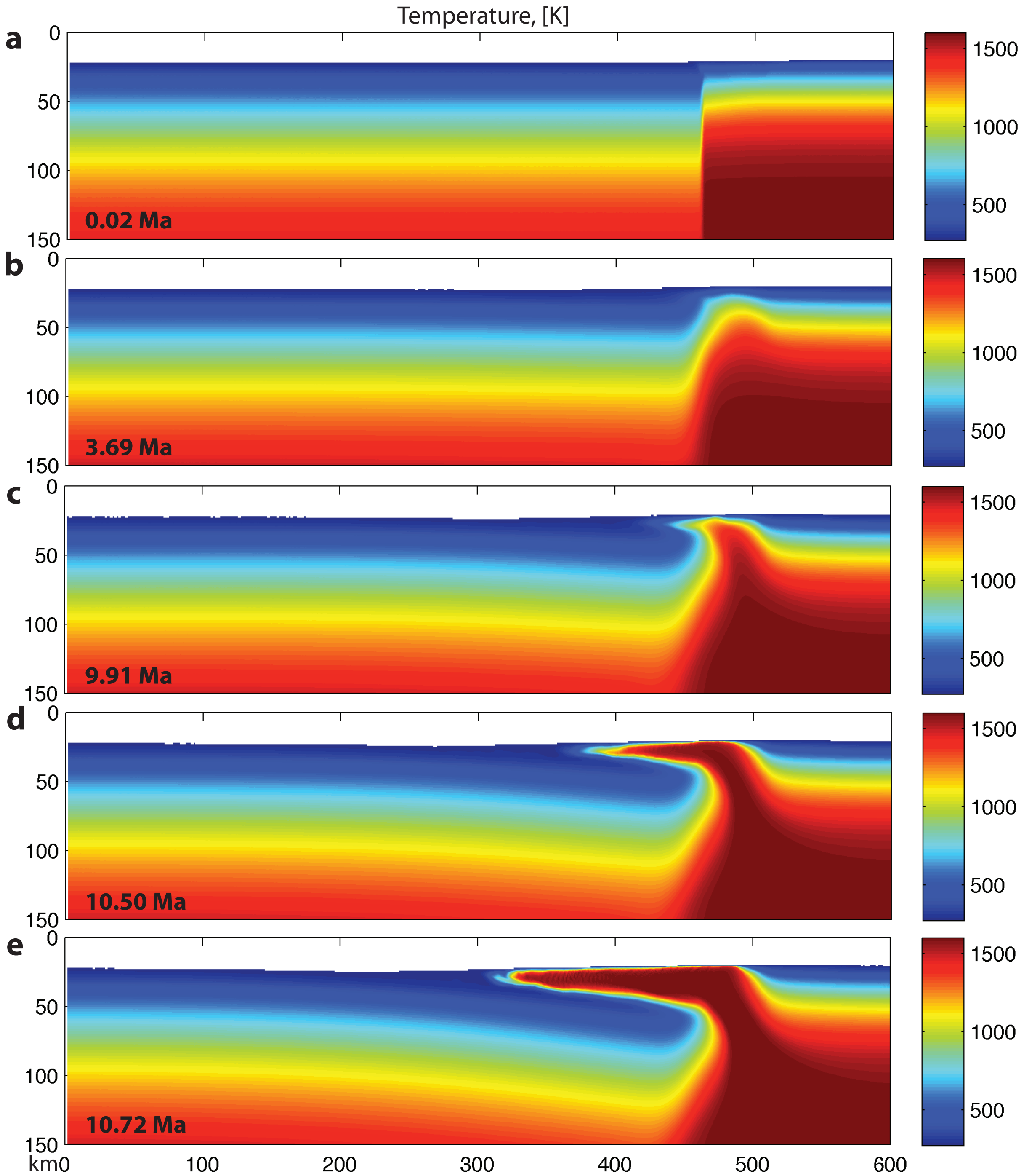

Figure S1: Evolution of the temperature field for the model development of Fig. 2. **a.** Temperature is initially distributed according to the cooling ages of the plates *Turcotte and Schubert* [2002], is equal to 273 K on the surface and reaches the value of 1600 K in the astenospheric mantle. **b.-e.** Hot asthenospheric mantle gradually overrides bending older oceanic plate forming the slab.

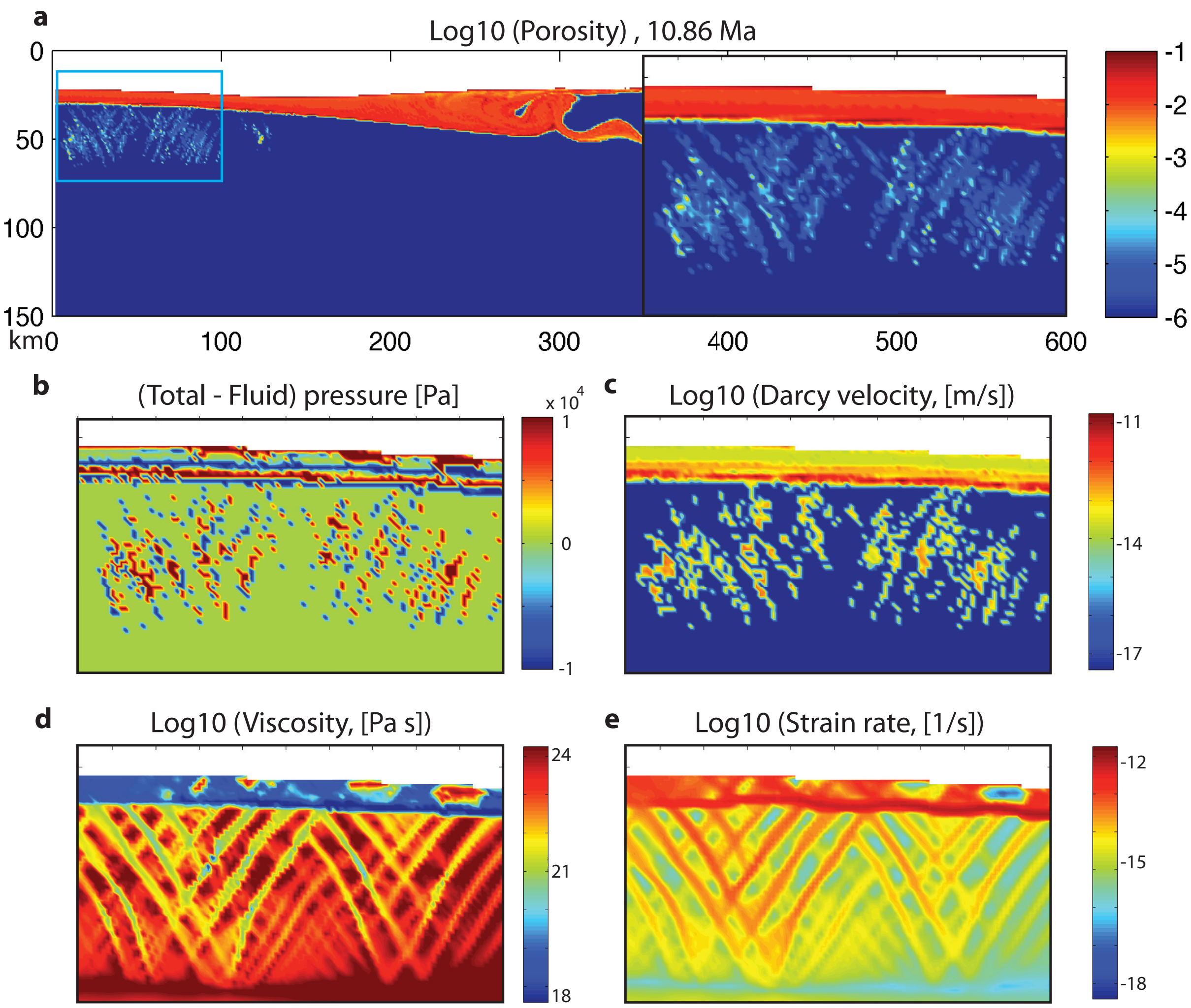

Figure S2: Fluid downward suction into the normal faults formed in the slab bending region. **a.** Porosity diagram: opening of the pore space inside the shear zones. **b.** Difference between total and fluid pressure; narrow limits of colormap are imposed to increase the visibility of the fluid overpressure zones (blue color). **c.** Darcy (fluid filtration) velocity: fluid percolation inside the faults. **d.** Viscosity diagram with normal faults marked by the zones of lowered effective shear viscosity. **e.** Strainrate diagram.

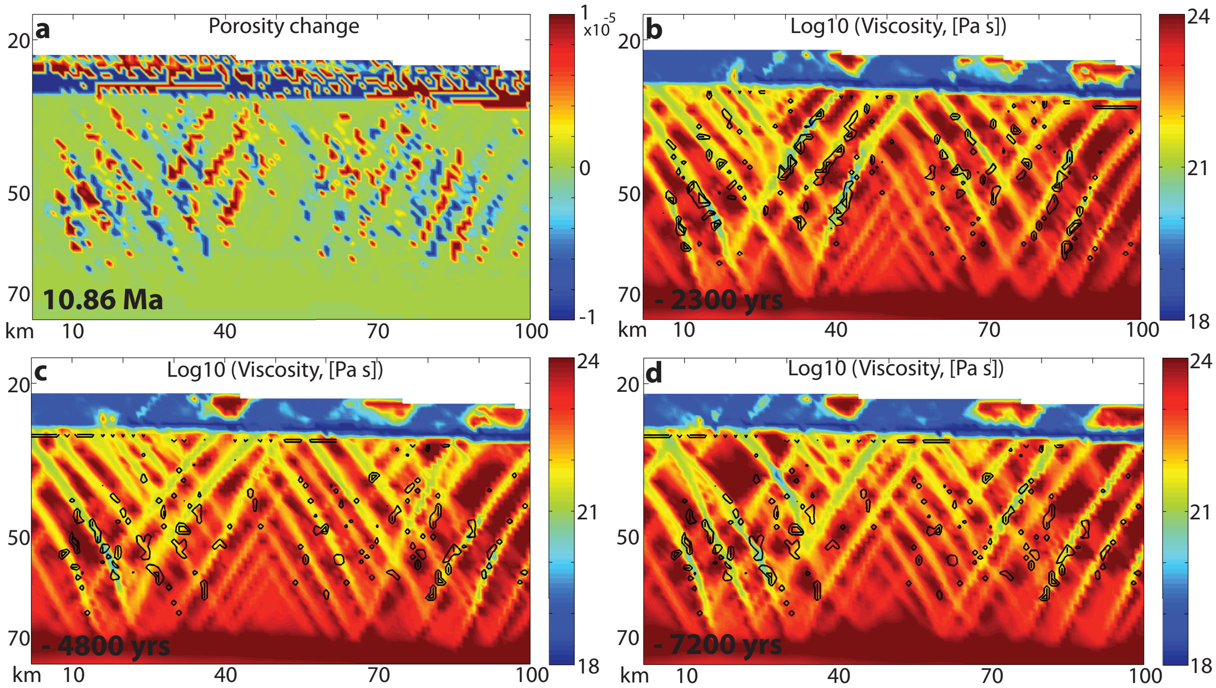

Figure S3: Evolution of porous space inside the normal faults at the time moment of 10.86 Ma (Fig. S3). **a.** Porosity change between two time moments (present and -2300 yrs). Color limits of the diagram are intensified for the better visibility. Red zones signify opening of the porous space, blue zones imply pore closure. **b.** Viscosity diagram with normal faults distribution for the previous time moment (-2300 yrs). Black contours stand for the red areas from the diagram **a** which signify opening of the pores getting filled with fluid. One can see that pore space opening happens inside the faults. **c. - d.** Viscosity diagrams with normal faults distribution for two earlier moments of time (-4800 and -7200 yrs). Black contours signify blue areas from the diagram **a** which mean porous space closure. One can see that the previously open fluid filled pores are collapsing after faults location is shifted.